Carbon 186 (2022) 437–451

Contents lists available at ScienceDirect

Carbon

journal homepage: www.elsevier.com/locate/carbon

Synthesis of pristine graphene-like behaving rGO thin film: Insights into what really matters

Mohammed Sedki [a], Pegah S. Mirabedini [a], Kenta Nakama [b], Garrett Stephens [c], Michael Groves [c], Ilkeun Lee [d], Mahesh R. Neupane [a, e, **], Ashok Mulchandani [f, g, *]

[a] Materials Science and Engineering Program, University of California, Riverside, CA, 92521, USA
[b] Department of Biotechnology and Life Science, Tokyo University of Agriculture and Technology, 2-24-16 Naka-cho, Koganei, Tokyo, 184-8588, Japan
[c] Department of Chemistry, California State University, Fullerton, CA, 92831, USA
[d] Department of Chemistry, University of California, Riverside, CA, 92521, USA
[e] DEVCOM Army Research Laboratory, 2800 Powder Mill Rd, Adelphi, MD, 20783, USA
[f] Department of Chemical and Environmental Engineering, University of California, Riverside, CA, 92521, USA
[g] Center of Environmental Research and Technology, University of California, Riverside, CA, 92507, USA

ARTICLE INFO

Article history:
Received 20 July 2021
Received in revised form
16 September 2021
Accepted 5 October 2021
Available online 12 October 2021

Keywords:
Reduced graphene oxide (rGO)
Field-effect transistor (FET)
rGO-FET
Pristine graphene
DFT calculation of graphene oxide
Impact of lateral size

ABSTRACT

Despite the huge expansion of GO/rGO market, there is a clear lack of experimental studies on getting high quality, large scale GO and rGO nanosheets/thin films, which is a critical requirement for electronic applications. In this work, a detailed experimental study on the effect of lateral sheet size on properties of GO/rGO, supported by density functional theory (DFT) calculations, is presented for the first time, to help prepare pristine graphene-like rGO. Furthermore, we investigated the effect of thermal reduction at low temperature (200 °C), under ambient pressure, on the corresponding electronic properties of rGO. Current-voltage (I–V) analysis, optical and electron microscopy, atomic force microscopy, Raman, XPS, and quantitative ^{13}C NMR spectroscopy were used to study and optimize rGO. The optimized rGO-field-effect transistor (rGO-FET) device exhibited the highest charge carrier mobilities, i.e. 2,962 (holes) and 2,183 (electrons) $cm^2/V.s$. Furthermore, the transconductance characteristic curve of rGO-FET showed the ambipolar behavior of high-quality graphene, with Dirac point around zero. In addition, the optical band gap of rGO nanosheets (~0.4 eV), prepared in this work, is among the smallest reported band gaps for rGO. These findings highlight the significance of our study for synthesizing large-scale graphene-like rGO thin film, for ultra-fast, low-power transistor applications.

1. Introduction

Graphene is a two-dimensional (2D) one atom-thick layer of carbon atoms packed in a honeycomb hexagonal lattice, with very attractive mechanical, electrical, thermal, and optical properties [1]. It has a high intrinsic mobility of 200,000 $cm^2/V.s$, high thermal conductivity of ~ 5000 W/m.K, and large specific theoretical surface area of 2630 m^2/g [1–3]. Due to its superior properties, graphene and its derivatives are widely used in a wide range of applications, including batteries [4,5], liquid crystals [6], hydrogen storage [7], field emission cathodes [8], organic photovoltaics [9], transistors [10], reinforcing polymers [11], water membranes [12], etc.

Chemical vapor deposition (CVD) and molecular beam epitaxy (MBE) are getting more attention as versatile bottom up techniques in synthesis of high-quality graphene for electronic applications, compared to liquid phase exfoliation (LPE) [13]. Despite being environmentally friendly and having a potential for large scale production of graphene, LPE produces low yield (especially for the monolayer sheets), small flake size (<5 μm), limited dispersibility, etc. [14]. Among many approaches, chemical exfoliation of graphite into graphene oxide (GO) and then its reduction to reduced graphene oxide (rGO) is one of the promising mass production routes of graphene [15,16]. GO solves many of the problems of the CVD-, MBE-, and LPE-prepared graphene, as it is economic and easy to scale up with the desired functionalities, and it achieves high

* Corresponding author. Department of Chemical and Environmental Engineering, University of California, Riverside, CA, 92521, USA.
** Corresponding author. Materials Science and Engineering Program, University of California, Riverside, CA, 92521, USA.
E-mail addresses: Mahesh.r.neupane.civ@army.mil (M.R. Neupane), adani@engr.ucr.edu (A. Mulchandani).

https://doi.org/10.1016/j.carbon.2021.10.011
0008-6223/

dispersibility of small and large flakes as well as high yields of monolayer sheets [1,15,17]. It can also be used to form stable graphene thin films [18] by means of drop casting, spin coating, or spraying GO suspension to the target surface, and *in situ* reducing it to rGO/graphene thin film at low temperatures. In addition, the reduction of GO can be controlled to prepare graphene materials with tunable band gaps [19]. Therefore, rGO is an excellent source of graphene.

Nevertheless, GO remains an elusive material [20,21] and there is a huge variation in the properties of the graphene produced by oxidative exfoliation. There are many recent reports on GO/rGO nanosheets and their composites, however, there exists an overwhelming consensus among researchers on the lack of high-quality, electronic-grade graphene on the market [22,23]. Furthermore, the physicochemical and electrical properties of graphene vary widely due to the lack of fundamental understanding of factors determining the quality of graphene thin films produced from the rGO nanosheets, limiting their usage in electronic applications, particularly in field-effect transistor (FET) systems. A recent promising study conducted by Kauling et al. on the LPE graphene from 60 producers demonstrated that there is a huge variation in the quality of produced graphene on market, and they introduced a systematic and reliable protocol to test graphene quality, which should help the market move faster and more efficiently with this method [22].

To the best of our knowledge, there is lack of studies on the main contributing factors in production of high quality rGO thin films that exhibit pristine graphene-like properties. This work also aims at revealing the factors that really matter for producing pristine graphene-like behaving rGO thin film. The number of stacked layers and thickness of drop casted rGO film play a role and hence we kept them uniform through the whole study to understand the effect of other contributing factors. Among many contributing factors, we found that lateral sheet size of GO/rGO, that is defined by the lateral size of the starting graphite flakes, plays a crucial role in the electronic properties of rGO nanosheets, rGO thin films, and their corresponding FET devices.

In this work, we have studied the effect of lateral sheet size on the electronic properties of the corresponding thin films of rGO. The experimental measurements were supported by density functional theory (DFT) calculations. In addition, we studied the effect of thermal reduction on the chemical composition of the large and small GO nanosheets synthesized by improved Hummers' method (IHM) [24] at low temperature (200 °C), under ambient pressure, which allowed for more insights into the effect of lateral sheet size on the electronic properties of rGO thin films. All electrical measurements were done via rGO-FET, using gold interdigitated electrodes (IDE). The optimized rGO nanosheets showed the smallest optical band gap (0.4 eV) and the highest charge carrier mobilities reported for rGO, to-date. Furthermore, FET characteristic curve of rGO-FET showed the nice ambipolar behavior of high-quality graphene, with Dirac point around zero. These results highlight the importance of this study for both researchers and companies aiming at using rGO for electronic applications.

2. Experimental details

Materials. Graphite powder (0.2 μm), potassium permanganates ($KMnO_4$, 99%), phosphoric acid (H_3PO_4, 85%), sulfuric acid (H_2SO_4, 98%), hydrochloric acid (HCl, 37%) and hydrogen peroxide (H_2O_2, 30%) were procured from Fisher Scientific, USA. Graphite powder (1–2 μm) and (3-Aminopropyl) triethoxysilane (APTES) were purchased from Sigma (St. Louis, MO, USA). Graphite flakes 7–10 μm and 40 μm (325 mesh) were bought from Alfa Aesar (Ward Hill, MA, USA). For the 0.2 μm graphite, it is labeled by the manufacturer as graphite powder. From our characterizations, including atomic force microscopy (AFM) imaging, the lateral size was found <1.0 μm with an average of 0.2 μm. The 40 μm sample is labeled by the manufacturer as graphite flakes −325 mesh.

Synthesis of GO nanosheets. GO nanosheets were prepared using the improved Hummers' method (IHM) [24], with some changes in reaction temperature and time, as we previously reported [25]. Briefly, 1 g of graphite powder was added to a mixture of 13 mL of phosphoric acid 98% and 120 mL of sulfuric acid 98%, and left under magnetic stirring for half an hour at room temperature. Then, 6 g of potassium permanganate was added portion-wise to the homogenized mixture. The reaction temperature was elevated to 45 °C and the reaction mixture was kept stirring for 3 h. The reaction was stopped by slow and cautious pouring of the reaction mixture to a beaker, in ice, containing a mixture of 150 mL of deionized (D.I.) water and 20 mL of hydrogen peroxide. Excess D.I. water was added to the beaker and the mixture was kept static overnight to settle the prepared graphite oxide (GtO) nanosheets down and make it easy to decant the highly acidic supernatant. The prepared graphite oxide (GtO) sheets were washed several times with hydrochloric acid (5%) and D.I. water by centrifugation, and then with D.I. water to form graphene oxide (GO) nanosheets. Further exfoliation by sonication can be used, however, it is not necessary in this method. The sample was dried at 50 °C.

Fabrication of rGO-FET chips. Devices (chips) were microfabricated on a highly doped p-type silicon substrate with approximately 300 nm SiO_2 insulating layer deposited on top. Electrodes were patterned on the substrate by photolithography. Next, 5 nm Cr layer was deposited on the substrate, followed by a 50 nm layer of Au, using e-beam evaporation. Each chip had 20 interdigitated gold fingers (10 pairs), the width of each finger was 5 μm and was separated by a gap of 3 μm (Fig. 1a). Electrodes were then defined using a standard lift-off technique. Chips with patterned electrodes were cut from whole wafer, cleaned, and immersed in ammonia solution, for 1 h, to introduce hydroxyl groups. Next, chips were immersed in 3-aminopropyltriethoxy silane (APTES) for 1 h, to assist GO nanosheets immobilization. Then, 10 μL suspension of GO in D.I. water of different concentrations was drop casted to the five interdigitated electrodes. The GO drop was left to dry and form a thin film at room temperature, and then annealed at 200 °C for 120 min.

Characterizations. The prepared materials were characterized using scanning electron microscopy (SEM, ThermoFisher Scientific (formerly FEI/Philips) NNS450) and UV–Visible spectrophotometer. Raman spectra were collected by Horiba LabRam using a green laser ($\lambda = 532$ nm) for excitation with a power of 10 mW. X-ray photoelectron spectroscopy (XPS) characterization was carried out using a Kratos AXIS ULTRA^{DLD} XPS system equipped with an Al X-ray source and a 165-mm mean radius electron energy hemispherical analyzer. Samples were prepared as thick films (~1 mm) on gold-coated polyimide substrate. Vacuum pressure was kept below 3×10^{-9} torr during the acquisition. Data were acquired with a step size of 0.2 eV and 0.1 eV for the survey and the high resolution (C1s and O1s) spectra, respectively. Quantitative solid state single pulse ^{13}C magic angle spinning (MAS) NMR spectral analysis was performed using Bruker Avance NEO 600 MHz spectrometer. The samples were ground and packed into a 4 mm rotor. Then, samples were spun at 10 kHz for more than 3000 scans with a relaxation delay of 10 s. 7.2 μs 90-degree pulse excitation was used over a bandwidth of 150 MHz and we used solid adamantane (38.48 ppm) as the reference for ^{13}C spectrum based on the trimethylsilane scale. Electrical measurements were conducted using Keithley 2636 system.

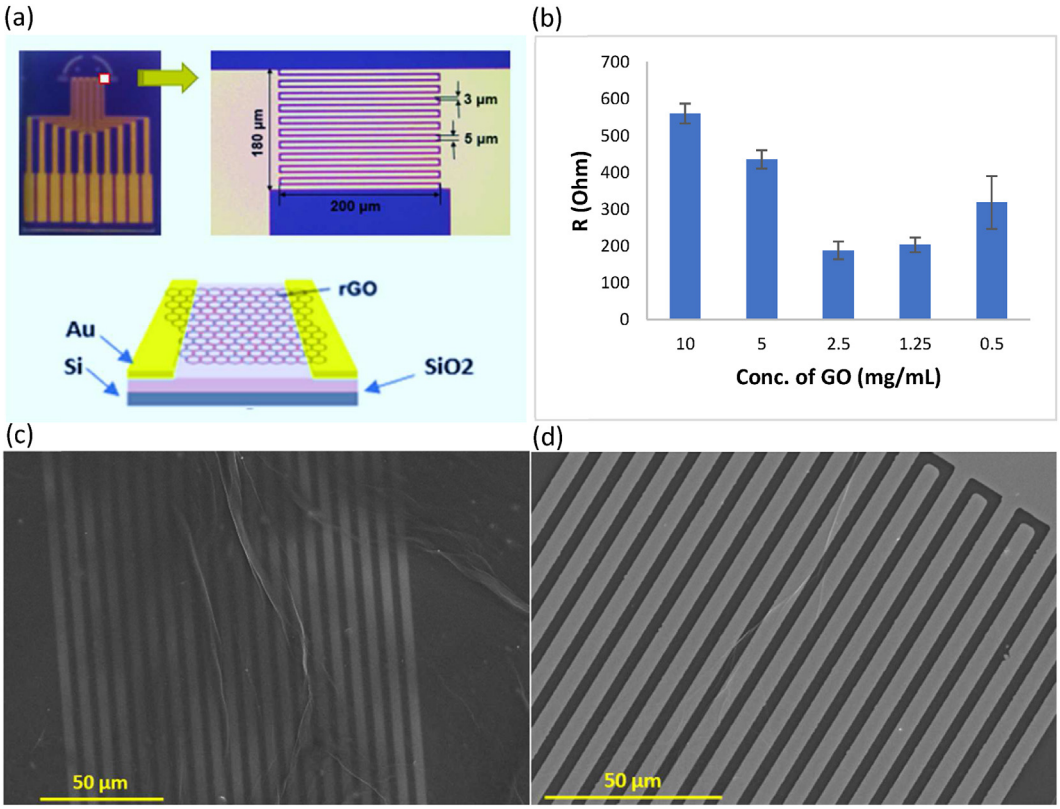

Fig. 1. (a) Camera image of the FET device of 5 IDEs (left), an optical microscopy image of one of the IDEs (right), and a schematic of rGO bridging two gold strips (bottom). (b) Effect of GO's concentration (mg/mL) on the device's resistance (Ohms). (c & d) SEM images of rGO-FET at 10 & 1.25 mg/mL, respectively. (A colour version of this figure can be viewed online.)

3. Results and discussion

GO was synthesized using IHM [24] with some modifications in reaction time and temperature, as we reported [26] in a previous work. Then, GO was thermally reduced at 200 °C, in open air, for 2 h. All electrical characterizations of rGO reported in this study were conducted via FET system. The configuration and channel dimensions of the gold interdigitated electrodes (IDEs) chip or the FET system are illustrated in Fig. 1a. Each IDE has 5 μm wide by 200 μm long gold strips/fingers electrodes separated by 3 μm (gaps) with a total working area of 180 × 200 μm [2]. Moreover, each chip has a set of 5 IDEs. rGO thin film is covering the whole working area, filling the channel gaps, and bridging the gold strips to close the circuit, as illustrated in the schematic of Fig. 1a. A simple and efficient preparation method was developed so that a well-connected film of rGO was formed on top of the gold IDEs resulting in formation of rGO-FET devices. Briefly, 10 μL of GO suspension, with different concentrations, were drop casted to the working area of IDEs, warmed to dry, and then thermally reduced at 200 °C in oven, under ambient pressure. The effect of concentration of GO, at a fixed volume of 10 μL, on the resistance/transport characteristics was studied. Scanning electron microscopy (SEM) imaging was used to investigate the concentration and quality of the rGO thin film on gold IDEs. SEM images, Fig. 1c & d, show that a thick film with folding/wrinkles was formed at the 10 mg/mL, while a nice transparent and flat thin film of rGO was formed at the concentration of 1.25 mg/mL. Additional SEM images for other concentrations are available in supplementary information (SI) Fig. S1. As illustrated in Fig. 1b, the device's resistance decreased by decreasing GO's concentration from 10 mg/mL to 2.5 mg/mL, stabilized at 1.25 mg/mL and then increased again upon decreasing the concentration below 1.25 mg/mL. Hence, the recommended concentration for use in rGO-FET system preparation is 1.25 mg/mL.

In general, the FET characteristics in the nano-scaled device are determined by the quality of the constituent device elements such as channel, contact and gate. The factors that influence the device characteristics include: 1) properties of channel material, in this case rGO, such as lateral size, and quality of the deposited graphene sheets [27]; and 2) channel length [28] and applied source-drain potential. In our study, we focus on the impact of lateral sheet size on properties of rGO, while keeping other parameters/factors constant. It is worth mentioning that the lateral sheet size of rGO is taken to be the lateral size of starting graphite.

3.1. Oxidative exfoliation

The electrical conductivity in graphite is an anisotropic property, and the larger the number of stacked layers, the bigger is the interlayer charge screening and scattering [29]. It is worth mentioning that most of the graphite flakes/powders available in the commercial market have wide range of sheet sizes in the same sample. For example, the 40 μm product had sheets ranging from 5 to 40 μm, with a majority between 15 and 20 μm; it was the same observation for 0.2, 2, and 10 μm sizes. Lateral sizes and thickness distributions of the four GO samples are shown in SI, Fig. S2. Hence, we have adapted centrifugation to remove the very small and very large sheets. All the four different size GOs, used in the resistance comparison, were investigated for their level of exfoliation using atomic force microscopy (AFM) imaging. The results in Fig. 2(a–d) show that the thickness of the GO nanosheets in 0.2, 2, 10, and 40 μm lateral size samples is uniform at ≈1.2 nm, which corresponds to monolayer GO nanosheets [30,31]. The equal number of

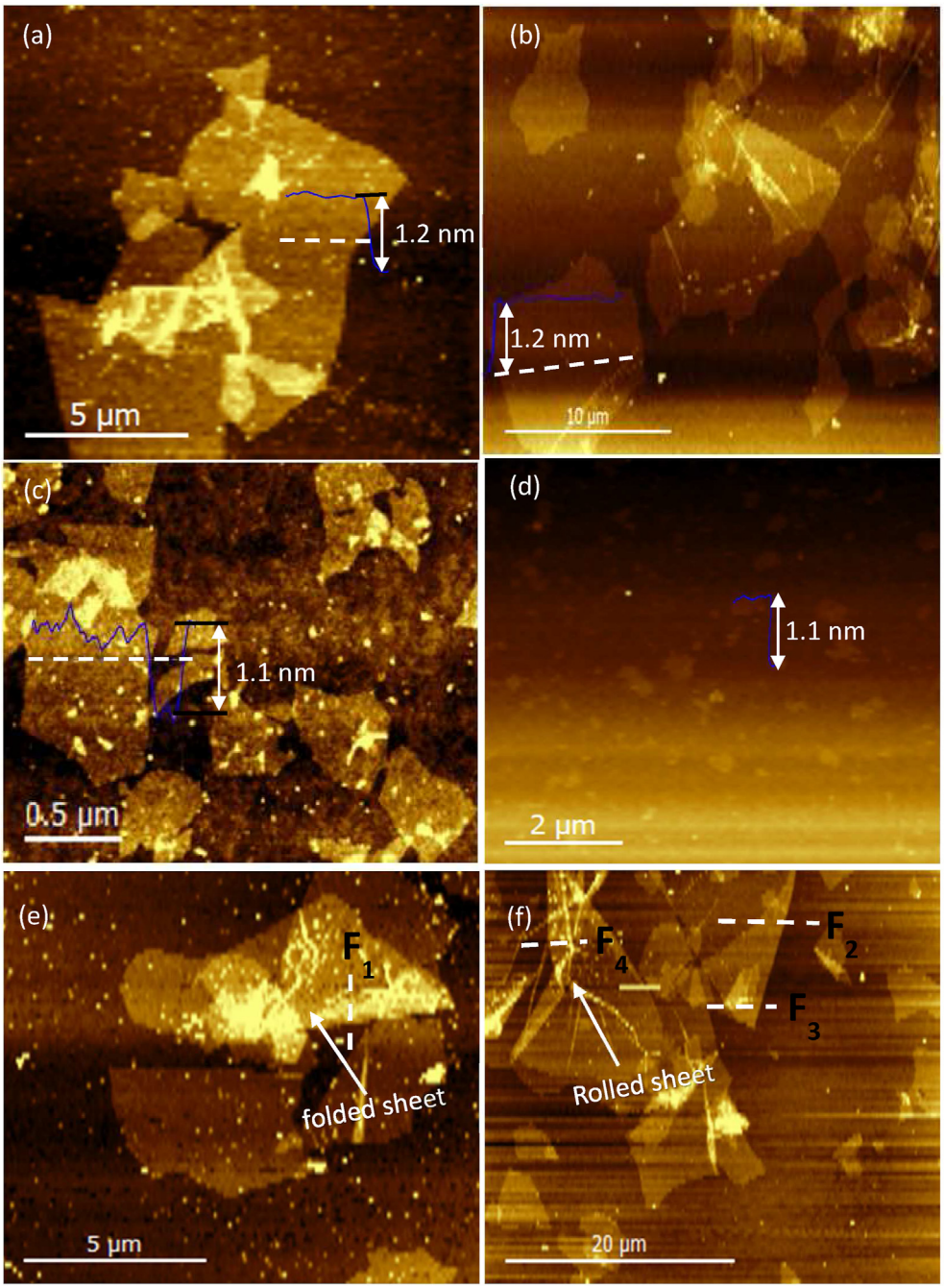

Fig. 2. AFM images of GO nanosheets with different sizes; (a) 40 μm, (b) 10 μm, (c) 2 μm, and (d) 0.2 μm samples. All samples were dispersed on a clean Si/SiO_2 substrate. Sheets larger than 10 μm tend to fold (e & f) when drop casted from their suspension. (A colour version of this figure can be viewed online.)

layers in the four GO samples confirms that the variation in resistance can be attributed to lateral sheet size effect and not due to the difference in exfoliation. Another important observation was that the sheets larger than 10 μm lateral size tend to fold, Fig. 2(e and f). This correlation between sheet size and folding is reported for the first time. However, the sheet folding problem in general was discussed in a recent report, and it can be explained by the compressive stress on the very flexible GO nanosheets during solution processing and deposition to substrates [32,33]. When the sheet first touches the substrate, it binds to it from one edge and then either to flatten on the surface in a way the other edges bind to substrate or to fold or roll around itself [34]. We believe that is attributed to the mechanical properties of the graphene sheets, especially their bending stress that increases by increasing the lateral size of the sheet, and hence makes it easier to fold and roll.

3.2. Lateral sheet size

To study the effect of lateral sheet size on device resistance, a potential of 0.1 V was applied between the source and drain of the rGO-FET devices made of thin films of different lateral sizes of rGO and the corresponding resistance was measured (Table 1). A bimodal linear correlation between the sheet size and device conductivity is evident from the tabulated data; a clear decrease in

Table 1
Correlation between lateral sheet size and thin film rGO-FET device's resistance, N = 10, where N is the number of pair electrodes.

Lateral sheet size (μm)	Resistance (Ohms)
0.2	700,000 ± 1000
2.0	800 ± 50
10.0	220 ± 18
40.0	200 ± 20

resistance with the increase in rGO lateral size from 0.2 to 10 μm and a very minor decrease in larger sizes such as 40 μm. The latter can be ascribed to the folding and rolling of the nanosheets larger than 10 μm, as seen in Fig. 2 (e & f). The folding/rolling was quantified using AFM imaging, by measuring the sheet height at the folding/rolling sites and found it 2.1, 2.3, 2.8, and 3.7 nm at four (F_1–F_4) different sites (see Fig. **2 e&f**), with an average height of 2.73 ± 0.71 nm. This number counts for the thickness of two sheets in addition to the curvature of folding. The thickness of two GO sheets is around 2 nm, and hence the folding/rolling curvature is about 0.73 nm on average. This number is not high due to the high flexibility of GO as well as its large size that increases the compressive pressure and results in flattening of the folded/rolled sheets. Corresponding AFM height profiles of folded/rolled GO nanosheets are shown in Fig. S3. For the 40 μm lateral size sample, despite the folding that might increase the surface roughness of a few nanometers, the film continuity is still better, the number of interfaces/grain boundaries is less, and the contribution from edge defects is smaller. A detailed discussion of the effect of lateral size on edge defects is discussed in section 3.2.3. So, the net result was that the film made from the 40 μm sheets has a slightly lower resistance. To summarize, we attribute the decrease in the resistance with increasing lateral sheet size to the enhanced film continuity, the smaller surface/interface roughness scattering, and lower contribution from non-healable edge defects.

3.2.1. Film continuity and interface roughness scattering

Graphene films made from smaller rGO sheets have greater discontinuities, due to the larger number of grain boundaries, and in-turn exhibit more charge screening and interface roughness scattering due to the bridging of randomly distributed small sheets. On the other hand, larger sheets network better to the adjacent sheets and form a well-connected film. The optical microscopy images, Fig. 3a, show clear discontinuity and random orientation in a thin film of small rGO sheets (0.2 μm) on Si/SiO_2 surface. In comparison, large sheets (flakes) of rGO show well-connected thin film with fine wrinkles that are 10–20 μm apart, Fig. 3b, which secures good electron transfer between the gold electrodes with gaps of 10–20 μm.

It is well known that the increase in surface/interface roughness increases the charge scattering dramatically and reduces the device carrier mobility [35]. Hence, the surface roughness of thin films of rGO nanosheets of two different sizes (0.2 and 40 μm) were investigated by AFM scanning, Fig. 3c-f. The AFM image and height profile of 40 μm rGO thin film in Fig. 3(c and d) show some fine wrinkles that are spaced 10 μm apart, similar to the optical image in Fig. 3b. The wrinkles may be due to the difference in the thermal expansion coefficients between rGO and SiO_2/Si substrate, which was reported elsewhere in case of graphene on Cu substrate [36,37]. The surface/interface roughness between wrinkles was 4 ± 3 nm, and when the wrinkles are included, the surface roughness slightly increased to 6 ± 5 nm.

On the other hand, the film surface/interface roughness of the 0.2 μm rGO thin film was 104 ± 50 nm, as shown in Fig. 3(e and f). Therefore, the smaller the sheets, the more random the orientation and the larger the number of grain boundaries resulting in a higher surface roughness and charge scattering of the corresponding thin film. The huge difference in roughness between the two sizes explains part of the variation in the FET device's resistance.

3.2.2. Contribution from non-healable edge defects

The oxidation of graphene sheets at the edges results in breaking some of the aromatic rings, and hence formation of non-healable defects in the graphitic domains. Thus, the implementation of the sheets with larger lateral size may reduce the contribution of the edges to the whole sheet and improve the electronic properties of GO and rGO nanosheets. This hypothesis, along with the effect of this low temperature thermal reduction, were studied using Raman spectroscopy, high-resolution X-ray photoelectron spectroscopy (XPS), and quantitative solid-state magic-angle spinning (MAS) ^{13}C NMR. Further investigation was conducted using DFT calculations, see **section 3.4**.

The other important factor that determines the rGO-FET device performance is the quality of produced rGO nanosheets. The quality here refers to how close rGO is to the pristine graphene and how efficiently the sheets heal from defects. The main parameters that affect the rGO nanosheets quality include graphite oxidation and GO reduction (healing) processes. Please, see the detailed discussion of this part in SI, **section 2**.

Raman spectroscopy is a powerful tool for studying crystal defects. The defects in graphene oxide samples are assessed from the ratio of the intensities (I_d/I_G) [38] of defects-induced D band and C–C bond stretches [39] in the sp^2 domains, and G band that is arising from first order Raman scattering. Raman measurements were conducted to determine the defect changes in GO and rGO thin films for the two different sheet sizes (40 and 0.2 μm), Fig. 4. Large sheet GO (GO-L) has shown less defects (I_d/I_G = 0.92) compared to small sheets (GO-S) where I_d/I_G was 1.02. After thermal reduction for 120 min at 200 °C in air, both samples undergone a sort of self-healing process by restoration of the sp^2 domains and graphitization, which caused a decrease in the I_d/I_G ratios. The decrease in defects over thermal reduction is in a good agreement with literature [38,40–42]. Other studies report an increase in I_d/I_G ratio over thermal or chemical reduction, though [43–46]. As reported by *Paredes* et al., this result of higher defects after reduction is contradicting the anticipated result of restoration of aromaticity and graphitization, and the proposed interpretation by attributing that to a higher number of overall smaller sp^2 domains formation was also argued [47]. The evolution of edge and basal plane defects and vacancies as well as the presence of sp^3 carbons are responsible for the amorphization of GO/rGO and thus the increase in the I_d/I_G ratio. Examples of vacancies are the smaller and larger rings formation due to the removal of one or more carbons from the adjacent six-membered rings in the oxidation process and the formation of distorted domains of 5-, 7-, or 8-membered rings in the form of the double vacancy (5-8-5 rings) or the common 5-7-7-5 rings disorder known as Stone-Wales defect, in the reduction/healing process [42,48,49]. Hence, the degree of amorphization of graphite in oxidation can reverse the interpretation of D band; in amorphous structures, the increased intensity of D band is associated with a higher level of ordering, and not defects as in graphene/graphite [50]. Thus, the huge variation in synthesis protocols of GO and hence in its quality and proportions of oxygen functionalities in its basal plane, as well as the contribution from edge defects cause variation in quality and interpretation of GO's Raman spectra. In this work, GO was synthesized using IHM (using phosphoric acid) that results in a more intact graphitic basal plane with less defects [24]. Phosphoric acid plays an important role in protection of basal plane, where it reacts with surface hydroxyl groups and prevents further oxidation. Accordingly, the basal plane oxygen groups (e.g.

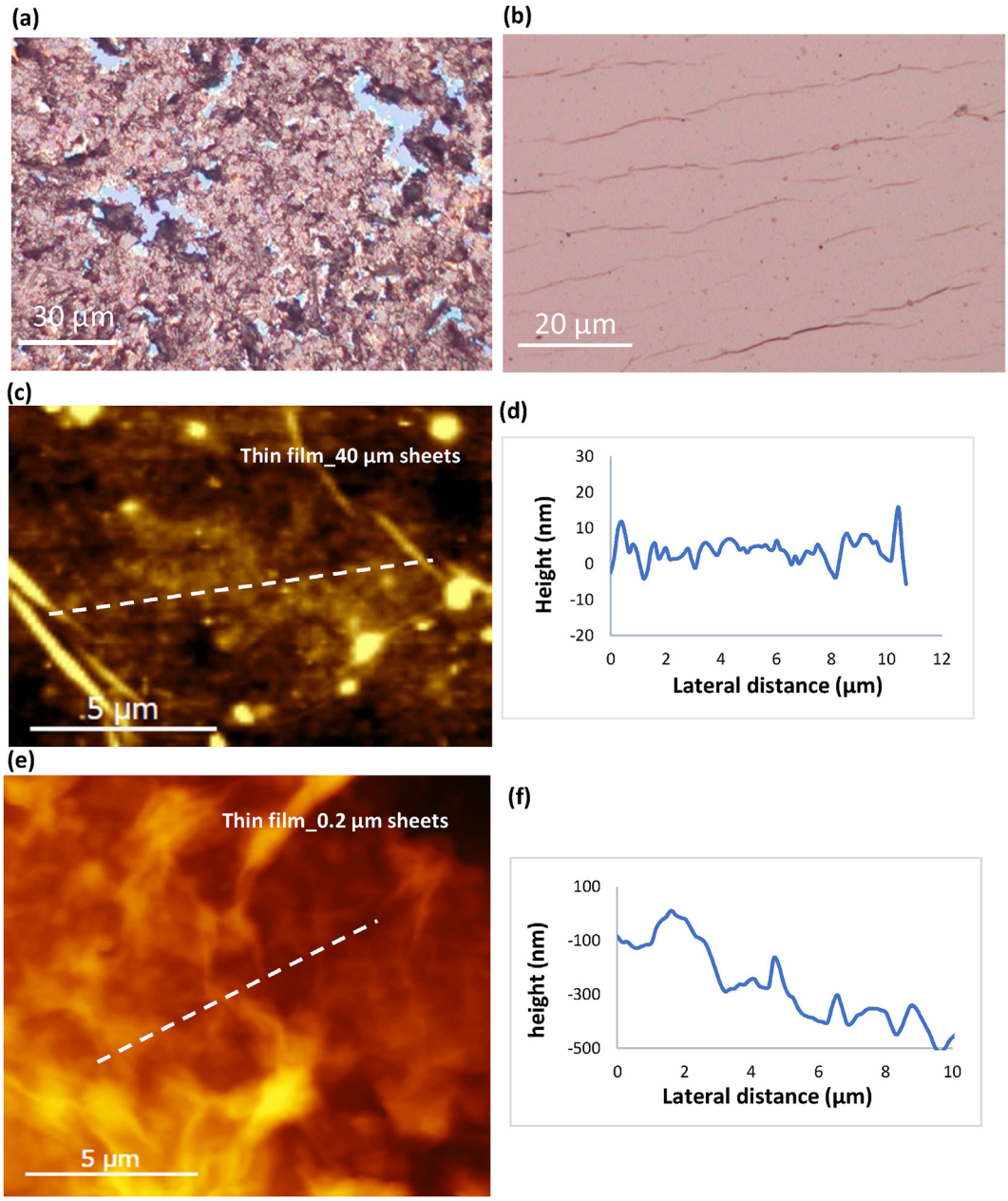

Fig. 3. Optical microscope images of thin films of (a) 0.2 µm rGO and (b) 40 µm rGO. AFM imaging (height images) and profiling of (c & d) 40 µm and (e & f) 0.2 µm rGO thin films on Si/SiO_2 substrate. (A colour version of this figure can be viewed online.)

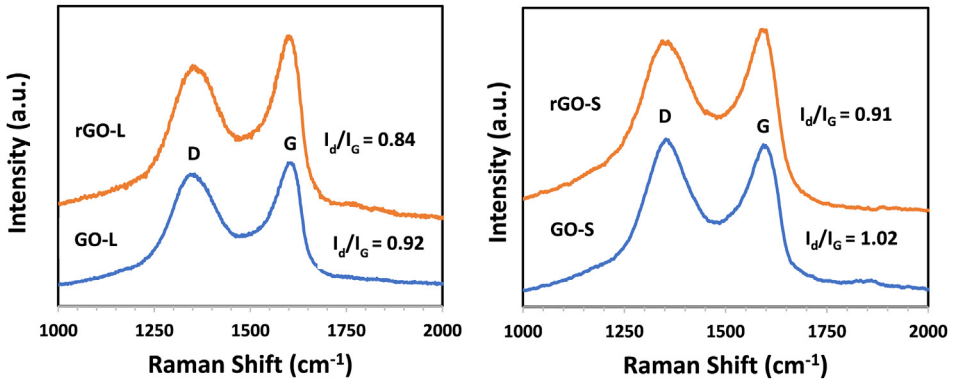

Fig. 4. Raman spectra of small and large sheets GO and rGO thin films. (A colour version of this figure can be viewed online.)

epoxy and hydroxyl) are less damaging when eliminated in reduction and leave less vacancies. Moreover, edge defects are higher in rGO-S (I_d/I_G: 0.91) than in rGO-L (I_d/I_G: 0.84).

Quantitative spectroscopic analyses of the chemical compositions of the large and small (i.e. lateral sheet size) samples of GO and rGO were carried out using XPS and quantitative MAS ^{13}C NMR. High resolution XPS was conducted on thick film samples of GO-S, GO-L, rGO-L, and rGO-S. The survey spectra of GO have shown only two distinct peaks of C1s and O1s, confirming the purity of the samples. After reduction, the survey spectra have shown a gradual decrease in the intensity of O1s peaks with time, Fig. S5. As shown in Table 2, the reduction process is clear from the significant increase in C/O ratio of large (L) and small (S) size graphene oxide samples from 2.45 and 2.33 to 4.26 and 4.55, respectively. To better understand the effect of this low temperature reduction on GO, and better explain the superiority of large sheets over small sheets, a detailed deconvolution process of C1s core level spectra was performed. Seven peaks were judiciously fitted, after a Shirley background subtraction, and were assigned to lattice vacancy defects (C–V) [51], sp^2-hybridized carbon atoms from aromatic domains (C=C), sp^3 carbons from aliphatic domains (C–C), hydroxyl and epoxy groups (C–OH and C–O–C), carbonyl (C=O), and carboxyl (COOH) groups, Fig. S6 and Fig. 5 [52,53]. All quantitative details of the changes in chemical compositions of the two (L & S) samples are shown in Table 2. The ratio of C=C/C–C has significantly increased from 5.38 (L) and 5.07 (S) to 19.29 (L) and 18.45 (S), which accounts for a strong restoration of aromatic graphitic domains. In addition, most of the reduction process is due to removal of C–O–C/C–OH groups from the basal plane. On the other hand, the percentage of C=O and COOH groups formed on the edges of GO/rGO has increased by thermal treatment at this low temperature, suggesting that a strong reduction process, by elimination of epoxy/hydroxyl groups, and a mild oxidation process, by forming new C=O/COOH groups, have occurred simultaneously [54]. Interestingly, the large sheets of GO and rGO had shown less carboxyl groups than the small sheets. Quantitatively, %COOH in GO-L was 2.78%, while in GO-S was 3.84%, i.e. GO-S has 16% more COOH groups than rGO-L, i.e. 16% more broken benzene rings at the edges of smaller sheets.

There is a considerable vagueness and subjectiveness in assigning and fitting XPS peaks of GO [53] arising from the huge disparities in literature due to the variation in structural models of GO (e.g. Lerf-Klinowski [55], Dekany[56], and Ajayan [57] models), which allows for different possible theoretical fittings of the XPS data. Hence, pursuing a quantitative MAS ^{13}C NMR [58,59] was very useful in determining the chemical compositions of rGO and supporting the accurate fitting of XPS peaks. The ^{13}C NMR results in Fig. 6 and Table 3 are in a good agreement with XPS results and highlight a strong reduction and mild oxidation processes happening concurrently. The epoxy and hydroxyl groups have been ~94% and ~96% eliminated, and the percentage of conjugated sp^2 carbons (C=C) has increased significantly from ~30% to ~ 60%, which explains the highly improved electronic properties of rGO (smaller band gap, lower resistance, and higher carrier mobility). The lower chemical shifts in the ^{13}C NMR spectra are attributed to the restoration of sp^2 conjugation in rGO [60]. The concentrations of COOH groups in GO-S and rGO-S are higher than that in GO-L and rGO-L, as shown in Table 3, which is aligning with the results from XPS data. The concentrations of COOH and C=O groups calculated from ^{13}C MAS NMR are slightly higher than those from XPS. This might be assigned to the higher sensitivity of ^{13}C NMR to the periphery groups of GO/rGO than XPS [57,61]. We believe the difference in sensitivity of ^{13}C NMR and XPS to functional groups at edges of GO/rGO nanosheets is due to the difference in the apparatus, where in the XPS measurement the X-ray beam shines perpendicularly on a horizontal spot of the sample that contains more contribution from basal plane than periphery. For ^{13}C NMR, the sample is grinded and stuffed into a rotor where the signal is collected from the whole sample more homogeneously and hence the edges have a better chance to be detected. Due to this higher sensitivity, the difference in %COOH between GO-S and GO-L became more significant; 3.13% for GO-L and 5.99% for GO-S, which means around 30% more broken periphery rings in GO-S.

More insights into the thermal reduction and lateral size effects based on Raman, XPS, and quantitative ^{13}C MAS NMR. Most of the oxygen functionalities are epoxy and hydroxyl groups in GO, and carbonyl and carboxyl in thermally reduced GO. Greatest amount of the C=O and COOH remaining in rGO may be distributed on edges and that is why XPS showed them in lower concentrations than ^{13}C NMR did. As per Lerf-Klinowski's [55] and Dekany's [56] models of GO, the most acceptable ones, COOH groups form only on edges. That supports our hypothesis of the formation of more non-healing edge defects in the small sheets due to their higher edges-to-core atoms compared to the large sheets, and helps explain one of the causes of the lower electrical conductivity and mobility, and higher Raman defects in rGO-S. The contribution of edge defects and their effects on band gap and electronic properties of rGO is discussed in more details in the computational model and calculations we present in this study.

The presence of higher C=O/COOH groups in rGO compared to GO, in general, is explained by the different proposed thermal reduction mechanisms [62–66], where the free hydroxyl and hydronium radicals formed from thermal decomposition of adsorbed water molecules attack the oxygen functionalities and convert some of them into C=O and COOH, and react further by removing them in the form of CO, and CO_2, preferentially at edges. As per Lipatov et al.'s work [62], the temperature programmed desorption measurements have revealed that the desorbed gases are mainly H_2O, CO, and CO_2. Part of the released H_2O desorbs at lower temperatures from the physically adsorbed water molecules, while the majority of the release peaks at the same temperature (~150 °C) where CO and CO_2 exhibit their maximum peaks, which confirms that this water has evolved from the removal of same type of groups that evolved as CO and CO_2. Other studies have reported the evolved gases as H_2O, CO_2, CO, H_2, O_2, and H_2O_2 [67–69]. That leaves behind restored sp^2 domains most likely from H_2O, H_2, O_2, and H_2O_2 removal, and edge defects and some etch holes from CO and CO_2 elimination. The electrical conductivity and electronic properties improved significantly when the aromatic domains grew enough to allow for percolative electronic transport that

Table 2
XPS quantitative analyses of the chemical compositions of GO-L, GO-S, rGO-L, and rGO-S.

	%C–V 283.1 ± 0.2	%C=C 284.5 ± 0.2	%C–C 285.1 ± 0.2	%C–OH 285.6 ± 0.2	%C–O–C 286.4 ± 0.2	%C=O 287.2 ± 0.2	%COOH 288.6 ± 0.2	C=C/C–C	C/O
GO-L	4.56	34.92	6.48	20.94	24.08	6.24	2.78	5.38	2.45
GO-S	4.87	33.22	6.54	20.43	25.10	6.01	3.84	5.07	2.33
rGO-L	0.62	63.27	3.28	11.07	6.07	9.77	5.92	19.29	4.26
rGO-S	0.83	60.84	3.29	10.29	6.21	10.61	7.94	18.49	4.55

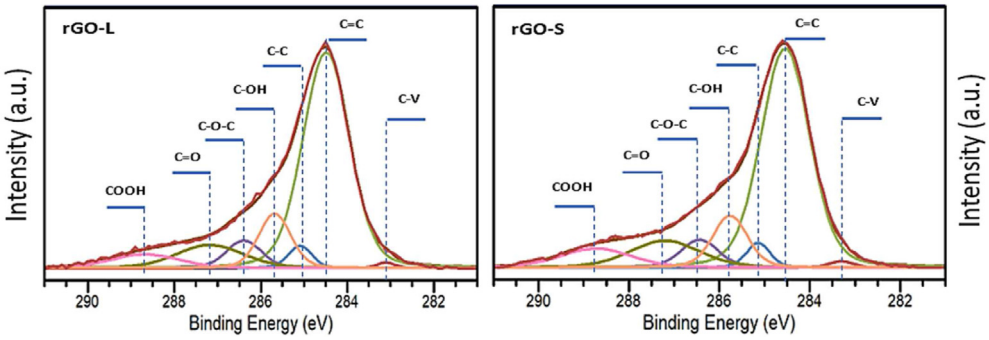

Fig. 5. High resolution C1s XPS spectra of reduced graphene oxide after 120 min reduction time at 200 °C in air. (A colour version of this figure can be viewed online.)

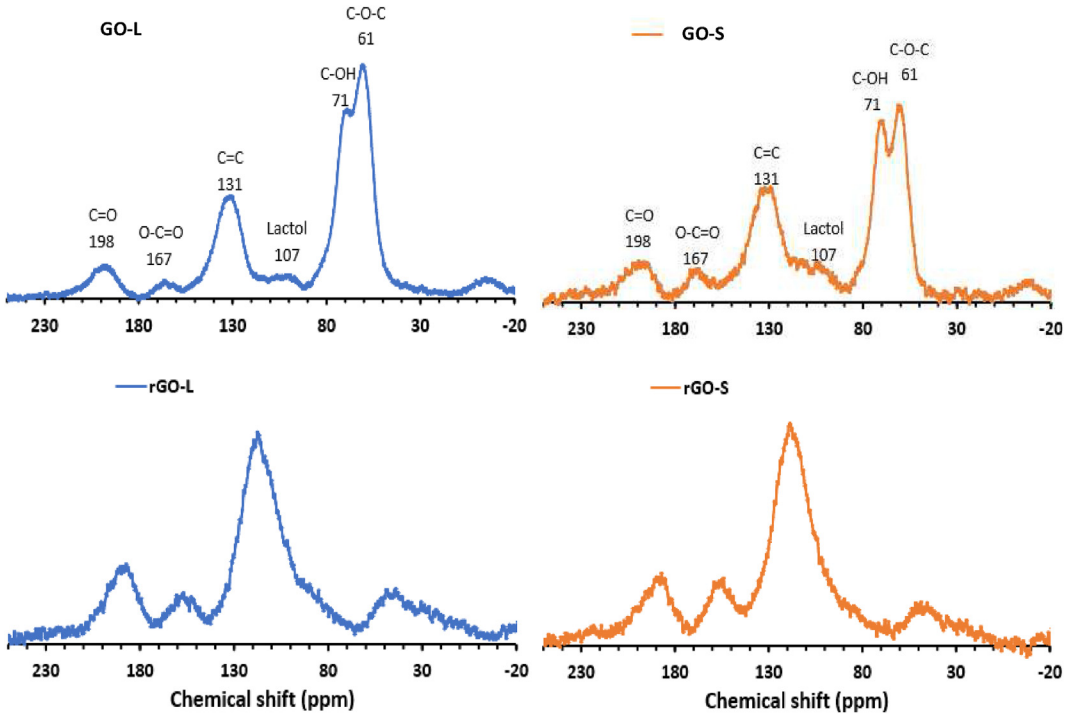

Fig. 6. Solid state magic-angle spinning ^{13}C NMR spectra of GO and rGO. (A colour version of this figure can be viewed online.)

Table 3
MAS^{13}C NMR quantitative analyses of the chemical compositions of GO-L, GO-S, rGO-L, and rGO-S.

	%Lactol	%(C=C)	%C–OH	%C–O–C	%C=O	%COOH
GO-L	2.71	28.04	23.52	34.45	8.16	3.13
GO-S	3.97	29.93	20.95	29.46	9.70	5.99
rGO-L	4.92	58.95	6.29	3.60	16.79	8.58
rGO-S	4.48	59.64	5.76	2.48	16.75	10.89

bypasses any possible etch holes. That explains the strong electronic properties enhancement after low temperature thermal reduction in air despite the presence of Raman defects. The Raman defects in rGO-S are slightly higher than defects in rGO-L, which can be attributed to the higher contribution from the non-healing edge defects.

3.3. Optical band gaps

For a better understanding of the significance of the reduction process in producing high quality GO/rGO nanosheets, changes in the optical band gaps (OBG) of GO/rGO were assessed from UV–Vis absorption spectra using Tauc's plot [70,71]. As previously reported, the band gap of GO/rGO is related to its carbon-oxygen ratio [72]. In other words, stripping oxygen functionalities from GO by means of reduction lowers its band gap. Furthermore, gradual restoration of graphitic structure and π conjugation by gradual reduction helps tune the band gap in a controlled manner. UV–Vis data and Tauc's plots of the 40 μm GO and rGO samples are presented in SI Fig. S7. Results in Table S1 show that at 0 min reduction, basically GO, the OBG is 1.8 eV, which is small compared to most of the reported band gaps of GO [73,74]. Hence, GO made by this optimized IHM method is less defected and highly exfoliated to monolayers, which makes it promising for getting high quality rGO nanosheets with a small band gap. In addition, the gradual reduction of GO resulted in a gradual decrease in the corresponding band gaps of rGO nanosheets, which is consistent with our theoretical results (discussed in section 3.4). Interestingly, after annealing/reduction for 120 min at 200 °C in air, the band gap of rGO reached 0.4 eV, which, to the best of our knowledge, is among the smallest values reported for

rGO [75]. This small band gap of rGO might be explained in terms of selection of the right size sheets (10–40 μm) that enables lower contribution of the less healable edge defects and the well-optimized oxidation and reduction methods.

3.4. First principle studies of GO and rGO sheets

To garner the fundamental understanding of the factors influencing the electronic properties of GO and rGO, we performed a set of density functional theory (DFT) calculations. The details on the methods and parameters used are provided in the SI document.

Among different GOs, epoxy and hydroxyl functionalized structures are known to be thermodynamically more stable, hence are chosen for this study [76]. Each bulk oxygen atom is bonded to its two neighboring carbon atoms to form an epoxy functional group, as illustrated in Figs. 7a and 8a. The epoxy and hydroxyl groups are added to both sides of the GO sheets to generate a more stable structure compared to their counterpart with functional groups only on one side. Both ends of the sheets are hydrogen (H-) terminated to mimic finite size effect. Hydrogenation is also a common method to convert the sp^2 to sp^3 hybridized carbon bonds and hence form a bandgap in graphene [76,77]. The structures are consistent with previous models of GO discussed elsewhere [77,78]. Details on the modeling of defected GO and rGO structures are discussed in the subsequent sections.

3.4.1. GO sheet size effect

To investigate the effect of sheet size on GO monolayer's electronic properties, we constructed structures with 4, 6, and 8 carbon layers labeled as Intact-A, Intact-B, and Intact-C, respectively (Fig. 7a). Carbon layers refer to the width of nanoribbon parallel to the periodic directions. Though the models representing the

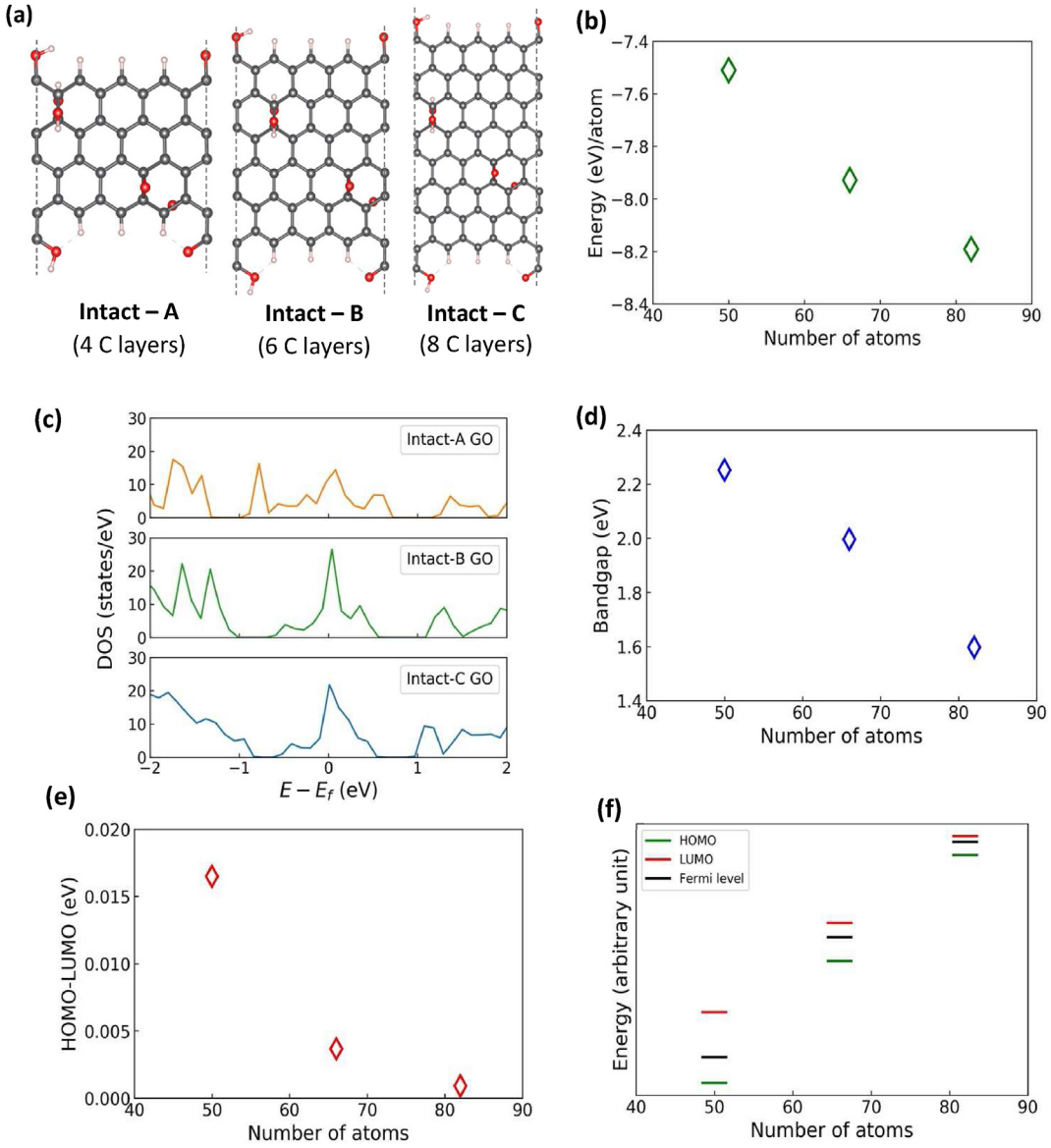

Fig. 7. (a) GO structures with 4, 6, and 8 carbon layers– intact A, intact B and intact C, respectively. Red, light red and gray circles represent O, H and C atoms, respectively (b) Total energy per atom plotted as a function of number of atoms in GO flake. (c) DOS plots of different-sized GO sheets. The sheet size increases from top to bottom. (d) and (e) Bandgap and HOMO-LUMO gaps as a function of GO sheet size, respectively, and (f) schematic evolution of electronic structure (HOMO, LUMO, and fermi level) for the three studied intact GO models, the dashed lines on left and right of plot (a) show the valence band maximum (VBM) and conduction band minimum (CBM), respectively. (A colour version of this figure can be viewed online.)

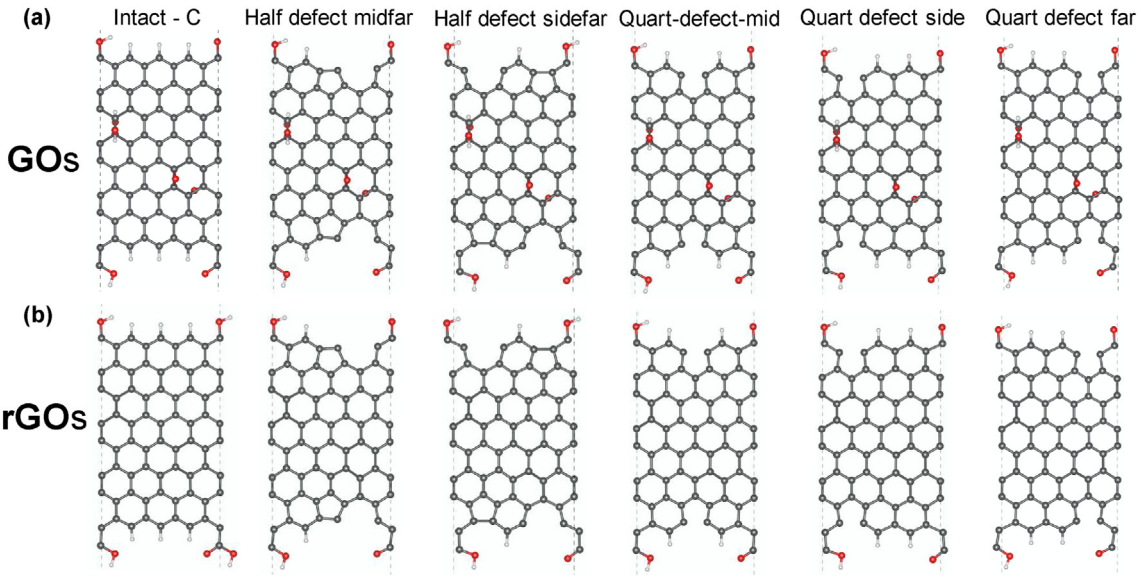

Fig. 8. Intact and defected atomic models of (a) GO, and (b) rGO models. Red, light red and gray circles represent O, H and C atoms, respectively The structures are labeled based on defect configuration. (A colour version of this figure can be viewed online.)

experimentally observed sizes are highly desirable, available computational resources limit the modeling of larger flakes. Hence, in this study, we have limited our model to the smaller ones (~1–2 nm). Regardless of the smaller finite sizes, our models exhibit GO behavior, and hence, can be used to predict the stability and electronic properties of larger GOs. Fig. 7b shows the ground-state energy per atom plotted as a function of GO size. The results show that the larger GO sheets are energetically more stable, which can be related to the reduction in the ratio of edge to bulk atoms as the sheet grows. In addition, the larger flakes tend to relax in-plane adsorbate induced strain efficiently as compared to smaller flakes, leading to relaively stable configurations. This behavior is also consistent with the experimental data.

Next, we studied the sheet size impact on the electronic properties of GO. Fig. 7c depicts the densities of states (DOS) plots for the three GO models. Increasing GO flakes' size reduces the band gap from 2.25 to 1.6 eV due to the reduction in the quantum confinement effect, as shown in Fig. 7d. Though the observed size-dependent band gap trend is unique, it is consistent with the recently reported O/C ratio dependent bandgap [79]. In this study, authors reported variation in the gap from 2 to 1 eV for the O/C ratio of 0.5 to 0.2, respectively. Quantitatively, our intact A, intact B and intact C models possess O/C ratio of 0.16, 0.12 and 0.1 with the band gap of 2.25, 2.1 and 1.6 eV, respectively. Here, we note that band gap's absolute value depends on many factors including the ratio of oxygen-to-carbon atoms [76], and the choice of exchange-correlation functionals. PBE functionals are well-known for underestimating the band gap. Regardless, our goal here is to draw a qualitative comparison with the experimental data, which is evident from the inverse relationship between the band gap and the sheet size. Fig. 7e shows the band gap between the highest occupied molecular orbital (HOMO) and the lowest unoccupied molecular orbital (LUMO), HOMO-LUMO gap, as a function of GO lateral size. As the sheet gets larger, the HOMO-LUMO gap becomes smaller. A schematic comparison of HOMO, LUMO, and fermi level for each model is presented in Fig. 7f, showing an increase in HOMO, LUMO, and fermi energy values, with the fermi level shifting towards LUMO as the GO sheet gets larger. Since the absolute energy values were small, we plotted these values in arbitrary units for better visualization. The corresponding calculated energy values are provided in Table S1. The observed reduction in the electronic band gap and HOMO-LUMO gap with the increasing GO size can be attributed to the reduction in the edge-state contribution to the band edges and quantum confinement effect [80] as well as a drop in the ratio of edge to core functional groups. Though the former argument does not hold true for the larger experimental samples, but the latter is valid, making the model developed in this study viable for larger samples. To the knowledge of authors, no previous studies have been reported on DFT calculations of size impact on GO/rGO properties. However, a similar size-dependent trend in electronic properties has been reported for MoS_2 [81] and silicon [82].

3.4.2. *Defects and reduction*

Modeling GO is an involved process. A variety of defected and reduced structures can be generated theoretically [76–78]. In experiments, the position of O and OH groups vary with processing method and conditions [76]. As optimizing defect and oxygen vacancy sites is outside the scope of this study, we limit our discussion to a few of such topologies with zigzag configurations. The purpose of this section is to investigate how defects and oxygen impurities, regardless of their configuration, affect rGO electronic properties. Fig. 8a depicts the atomic structure of intact and different defected GO flakes. Fully reduced GO models were generated by removing the core epoxy and hydroxyl functional groups.

DOS plots for intact and defected GO structures (Fig. 9a) show a decrease in the band gap and results in additional localized states appearing in the gap for all defected structures. Introducing edge defects involves breaking some of the sp^3 C–H bonds, increasing the number of unfunctionalized edge carbons with free orbitals, contributing to higher electronic conductivity, and lowering the bandgap. For half defect structures, the band gap is wholly removed. These are the structures with five-membered rings where the missing C–C bond increases the ratio of free orbitals, which lowers the band gap. To compare the stability and tendency of rGO sheets to oxidize, we calculated the relative formation energy (E_{RFE}) defined as the difference between the formation energy of GO and the corresponding rGO structure through **equation (1)** [76]:

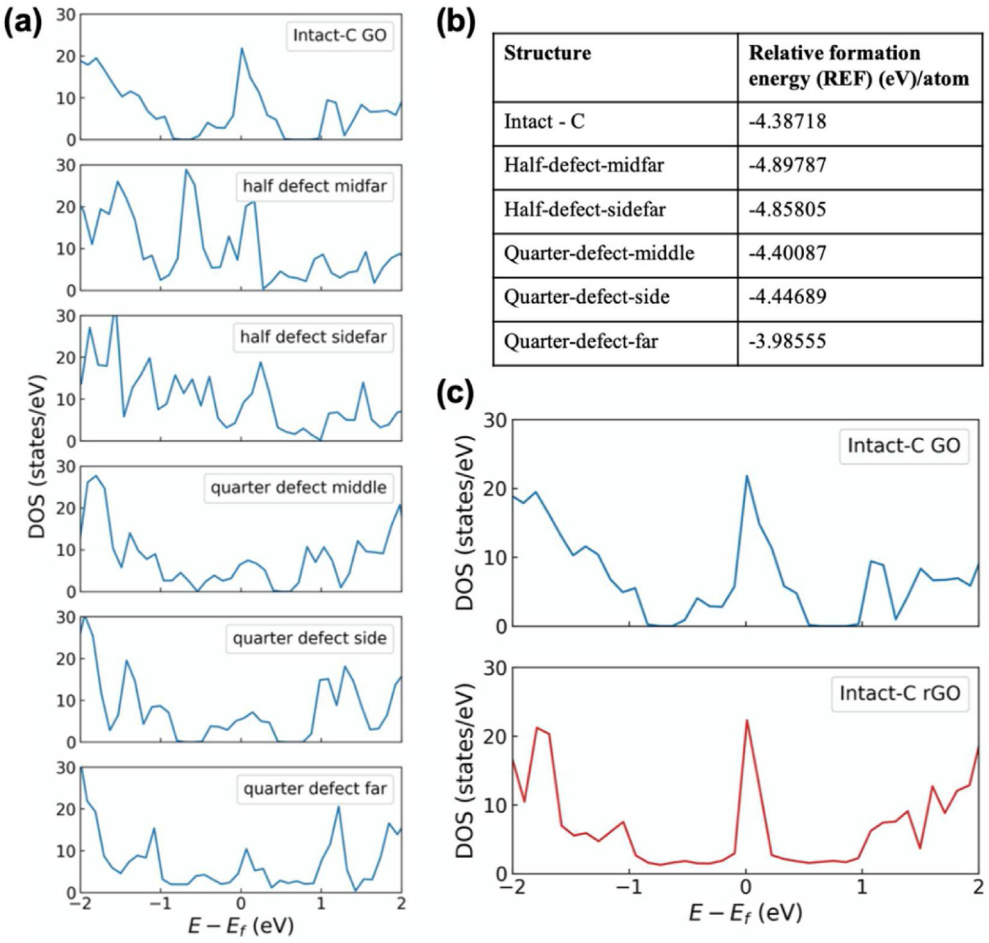

Structure	Relative formation energy (REF) (eV)/atom
Intact - C	-4.38718
Half-defect-midfar	-4.89787
Half-defect-sidefar	-4.85805
Quarter-defect-middle	-4.40087
Quarter-defect-side	-4.44689
Quarter-defect-far	-3.98555

Fig. 9. (a) Density of states (DOS) plots of intact-C and various defected GO structures (b) Computed relative formation energy (E_{REF}) values for the same structures. (c) The DOS plots for intact-C GO and rGO structures depicted for comparison. (A colour version of this figure can be viewed online.)

$$E_{RFE} = (E_{GO} - E_{rGO} - \Delta n_O \mu_O - \Delta n_H \mu_H) \quad (1)$$

Where E_{GO}, and E_{rGO} are the ground-state energies of GO and rGO, respectively. Δn_O and Δn_H refer to the difference in number of O and H atoms for the original and reduced structures, μ_O and μ_H are the chemical potential of oxygen and hydrogen, respectively. The table of E_{RFE} values is presented in Fig. 9b. The negative values of E_{RFE} indicate that oxidation makes all structures more stable. The lowest E_{REF} values belong to the half defect structures with five C rings which are expected to have higher reactivity due to their free orbitals.

Following the stability analysis, we performed site-project DOS for the intact-C GO and the corresponding reduced structures. Removal of epoxy groups results in appearance of sp^2 localized states distributing through the whole band gap of GO. The appearance of these states due to reduction is in line with previous study by Lundie et al. [77] Besides, based on our chemical intuition, since the rGO structures look more similar to pristine graphene compared to their GO opponents, they are expected to show higher electronic conductivity.

3.5. FET characteristics and charge carrier mobility of rGO thin film

The charge carrier mobility of the rGO nanosheets, after 120 min reduction time, was calculated from **equation (2)**, as reported elsewhere [10].

$$\mu = S \frac{L}{W} \frac{1}{Vsd} \frac{1}{Ci} \quad (2)$$

Where S is the slope in the linear part of the I_{sd}-V_g curve, L and W are the length and width of the channel, respectively, V_{sd} is the source-drain voltage, and C_i is the gate-channel (interfacial) capacitance. C_i was determined from the electrochemical impedance spectroscopy (EIS) and was found to be 1.48 μF/cm^2 , which is in a good agreement with literature [10,36]. Details of calculating C_i are in supplementary information, **section 4**.

Fig. 10(a-d) shows the FET characteristic curves using electrolyte-gating for rGO of 0.2 μm lateral sheet after 60 min reduction, and 40 μm sheet post 30, 60, and 120 min reduction. As shown in Fig. 10d, the FET curve of optimized rGO exhibit the ambipolar behavior of the pristine graphene. On the other hand, Dirac point of this rGO thin film is at ~ 0.01 V, which indicates that most of the p-type doping defects were removed, and its characteristics resemble pristine graphene like features where the Dirac point is located at the charge neutrality point.

The holes and electrons carrier mobilities of the optimized rGO-FET system were 2,962 and 2,183 cm^2/V.s, respectively. These values, to the best of authors knowledge, are the highest reported to-date for rGO-FET, LPE G-FET, and within the highest of the CVD G-FET (Table 4). It is worth mentioning that the mobility is directly proportional to the slope (dI/dV) of the FET transfer characteristics and hence it is directly proportional to the on-current. Since the on-

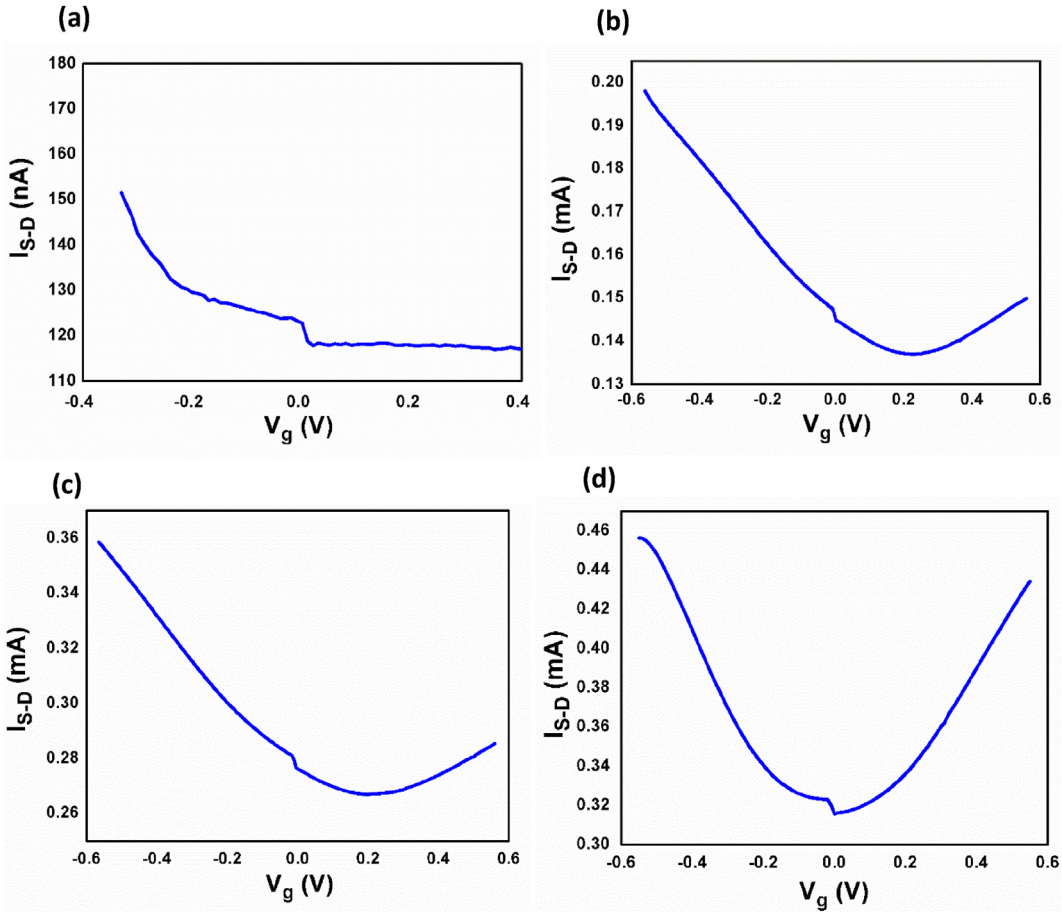

Fig. 10. The characteristic curves of rGO-FET system of 0.2 μm sheets after 60 min reduction (a) and of 40 μm sheets (a, b, & c) at different reduction times (30, 60, and 120 min) measured at 0.1 V between source and drain. The bias voltage was applied by top-gating with Ag/AgCl electrode and in 10 mM phosphate buffer saline (PBS) electrolyte. (A colour version of this figure can be viewed online.)

Table 4
Charge carrier mobilities of rGO- and CVD graphene (CVD G-) and LPE graphene (LPE G-) FET systems.

FET system	Mobility (holes) cm^2 /V.s	Mobility (electrons) cm^2 /V.s	Reference
rGO-FET	16	–	This work (before optimization)
rGO-FET	**2,962**	**2,183**	**This work (after optimization)**
rGO-FET	0.015	–	[83]
rGO-FET	82.5	27.5	[84]
rGO-FET	0.5	–	[85]
rGO-FET	2–200	0.5–30	[86]
rGO-FET	676	496	[87]
CVD G-FET	1,410	–	[88]
CVD G-FET	7.21	–	[37]
CVD G-FET	811	190	[89]
CVD G-FET	900	800	[90]
CVD G-FET	1,800	1,200	[91]
CVD G-FET	7,600	–	[92]
LPE G-FET	18.71	5.04	[93]
LPE G-FET	2.50	0.49	[93]

current in our rGO-FET devices is higher by an order of magnitude as compared to the previously reported state of the art devices (~0.4 mA vis-à-vis 0.001 mA), the mobility is expected to be significantly large compared to literature [48–56,58]. In summary, we attribute all these interesting pristine graphene-like properties observed in our rGO-FET devices to the high quality of the synthesized rGO nanosheets, the reduced surface roughness and charge scattering and the small contribution of the edge defects due to the right selection of the sheet's lateral size, as well as the good film continuity.

4. Conclusions

This work introduces a detailed experimental study, complemented by DFT modeling, of some of the critical factors affecting the quality of rGO nanosheets and thin films, and proposes a route to achieving pristine graphene-like rGO from the commercially available graphite. We observed that the lateral sheet size,

concentration and volume of GO solution, and quality of oxidation and reduction methods are the key factors in realizing a high-quality graphene-like rGO thin film. The optimized large rGO flake exhibits smallest reported optical band gap, lowest FET resistance vis-à-vis highest conductivity, and highest charge carrier mobility. The lateral size of the starting graphite has a significant impact on these properties of the corresponding rGO nanosheets. This observation is consistent with the thickness (lateral size) dependent reduction in the band gap predicted by the DFT method. The graphite flakes of lateral sizes 10–40 μm are more promising than powder graphite for electronic applications. The better performance of the larger size was attributed to the better film continuity, smaller roughness and smaller charge scattering, and lower contribution from non-healable edge defects. Raman, XPS and quantitative MAS ^{13}C results gave more insights into the effect of lateral sheet sizes and low temperature thermal reduction on the chemical composition of the film-forming nanosheets and hence the film's electronic properties. The rGO-FET device resistance decreased drastically by increasing lateral sheet size of the thin film rGO sheets from 0.2 to 2.0 and then to 10 μm, but the reduction in resistance plateaued for sizes larger than 10 μm due to the folding of larger sheets that was recorded using AFM imaging. We have also demonstrated that the modified IHM synthesis method is crucial for getting high quality and highly exfoliated GO nanosheets. During the reduction process, the reduction temperature was optimized to 200 °C, for 120 min at ambient pressure, which makes it facile method for *in situ* reduction of GO sheets or films on surfaces. In conclusion, a high-quality thin film of rGO sheets with graphene-like ambipolar transfer characteristics, a finite band gap of ~0.4 eV, and high holes (electrons) mobility of 2,962 (2,183) $cm^2/V.s$, might be useful in high-frequency, low power device applications, such as TFET, sensors and neuromorphic applications.

CRediT authorship contribution statement

Mohammed Sedki: Conceptualization, Methodology, Formal analysis, Investigation, Writing – original draft, Writing – review & editing, and Visualization. **Pegah S. Mirabedini:** Methodology, Formal analysis, Investigation, Writing – original draft, Writing – review & editing, and Visualization. **Kenta Nakama:** Investigation. **Garrett Stephens** and **Michael Groves:** Methodology, Conceptualization, Investigation. **Ilkeun Lee:** Investigation (XPS). **Mahesh R. Neupane:** Conceptualization, Methodology, Resources, Writing – review & editing, Supervision. **Ashok Mulchandani:** Conceptualization, Methodology, Resources, Writing – review & editing, Supervision, Project administration, and Funding acquisition.

Declaration of competing interest

The authors declare that they have no known competing financial interests or personal relationships that could have appeared to influence the work reported in this paper.

Acknowledgments

This work was generously supported by the National Science Foundation award number 1842718 and UC Riverside and Korea Institute of Materials Science (Research Program (POC2930)) through UC-KIMS Center for Innovation Materials for Energy and Environment. A.M. acknowledges the W. Ruel Johnson Chair in Environmental Engineering.

Appendix A. Supplementary data

Supplementary data to this article can be found online at https://doi.org/10.1016/j.carbon.2021.10.011.

References

[1] Y. Zhu, S. Murali, W. Cai, X. Li, J.W. Suk, J.R. Potts, R.S. Ruoff, Graphene and graphene oxide: synthesis, properties, and applications, Adv. Mater. 22 (35) (2010) 3906–3924.
[2] A.A. Balandin, S. Ghosh, W. Bao, I. Calizo, D. Teweldebrhan, F. Miao, C.N. Lau, Superior thermal conductivity of single-layer graphene, Nano Lett. 8 (3) (2008) 902–907.
[3] S.V. Morozov, K.S. Novoselov, M.I. Katsnelson, F. Schedin, D.C. Elias, J.A. Jaszczak, A.K. Geim, Giant intrinsic carrier mobilities in graphene and its bilayer, Phys. Rev. Lett. 100 (1) (2008) 16602.
[4] R. Chen, T. Zhao, T. Tian, S. Cao, P.R. Coxon, K. Xi, D. Fairen-Jimenez, R. Vasant Kumar, A.K. Cheetham, Graphene-wrapped sulfur/metal organic framework-derived microporous carbon composite for lithium sulfur batteries, Apl. Mater. 2 (12) (2014) 124109.
[5] J. Hassoun, F. Bonaccorso, M. Agostini, M. Angelucci, M.G. Betti, R. Cingolani, M. Gemmi, C. Mariani, S. Panero, V. Pellegrini, An advanced lithium-ion battery based on a graphene anode and a lithium iron phosphate cathode, Nano Lett. 14 (8) (2014) 4901–4906.
[6] M. Hegde, L. Yang, F. Vita, R.J. Fox, R. van de Watering, B. Norder, U. Lafont, O. Francescangeli, L.A. Madsen, S.J. Picken, Strong graphene oxide nanocomposites from aqueous hybrid liquid crystals, Nat. Commun. 11 (1) (2020) 1–7.
[7] V. Tozzini, V. Pellegrini, Prospects for hydrogen storage in graphene, Phys. Chem. Chem. Phys. 15 (1) (2013) 80–89.
[8] G. Viskadouros, D. Konios, E. Kymakis, E. Stratakis, Direct laser writing of flexible graphene field emitters, Appl. Phys. Lett. 105 (20) (2014) 203104.
[9] N. Balis, D. Konios, E. Stratakis, E. Kymakis, Ternary organic solar cells with reduced graphene oxide–Sb2S3 hybrid nanosheets as the cascade material, ChemNanoMat 1 (5) (2015) 346–352.
[10] C. Reiner-Rozman, M. Larisika, C. Nowak, W. Knoll, Graphene-based liquid-gated field effect transistor for biosensing: theory and experiments, Biosens. Bioelectron. 70 (2015) 21–27.
[11] G. Mittal, V. Dhand, K.Y. Rhee, S.-J. Park, W.R. Lee, A review on carbon nanotubes and graphene as fillers in reinforced polymer nanocomposites, J. Ind. Eng. Chem. 21 (2015) 11–25.
[12] Q. Yang, Y. Su, C. Chi, C.T. Cherian, K. Huang, V.G. Kravets, F.C. Wang, J.C. Zhang, A. Pratt, A.N. Grigorenko, Ultrathin graphene-based membrane with precise molecular sieving and ultrafast solvent permeation, Nat. Mater. 16 (12) (2017) 1198–1202.
[13] P. Capper, S. Irvine, T. Joyce, Epitaxial crystal growth: methods and materials, shep (2007) 271.
[14] A. Amiri, M. Naraghi, G. Ahmadi, M. Soleymaniha, M. Shanbedi, A review on liquid-phase exfoliation for scalable production of pure graphene, wrinkled, crumpled and functionalized graphene and challenges, FlatChem 8 (2018) 40–71.
[15] S. Pei, H.-M. Cheng, The reduction of graphene oxide, Carbon N. Y. 50 (9) (2012) 3210–3228.
[16] H. Feng, R. Cheng, X. Zhao, X. Duan, J. Li, A low-temperature method to produce highly reduced graphene oxide, Nat. Commun. 4 (2013) 1539.
[17] D.W. Boukhvalov, M.I. Katsnelson, Chemical functionalization of graphene, J. Phys. Condens. Matter 21 (34) (2009) 344205.
[18] M.M. MacInnes, S. Hlynchuk, S. Acharya, N. Lehnert, S. Maldonado, Reduction of graphene oxide thin films by cobaltocene and decamethylcobaltocene, ACS Appl. Mater. Interfaces 10 (2) (2017) 2004–2015.
[19] M. Acik, Y.J. Chabal, A review on thermal exfoliation of graphene oxide, J. Mater. Sci. Res. 2 (1) (2013) 101.
[20] E. Tegou, G. Pseiropoulos, M.K. Filippidou, S. Chatzandroulis, Low-temperature thermal reduction of graphene oxide films in ambient atmosphere: infra-red spectroscopic studies and gas sensing applications, Microelectron. Eng. 159 (2016) 146–150.
[21] A.M. Dimiev, T.A. Polson, Contesting the two-component structural model of graphene oxide and reexamining the chemistry of graphene oxide in basic media, Carbon N. Y. 93 (2015) 544–554.
[22] A.P. Kauling, A.T. Seefeldt, D.P. Pisoni, R.C. Pradeep, R. Bentini, R.V.B. Oliveira, K.S. Novoselov, A.H. Castro Neto, The worldwide graphene flake production, Adv. Mater. 30 (44) (2018) 1803784.
[23] P. Bøggild, The war on fake graphene, Nature (2018) 502–503, https://doi.org/10.1038/d41586-018-06939-4.
[24] D.C. Marcano, D.V. Kosynkin, J.M. Berlin, A. Sinitskii, Z. Sun, A. Slesarev, L.B. Alemany, W. Lu, J.M. Tour, Improved synthesis of graphene oxide, ACS Nano 4 (8) (2010) 4806–4814.
[25] M. Sedki, M.B. Mohamed, M. Fawzy, D.A. Abdelrehim, M.M.S.A. Abdel-Mottaleb, Phytosynthesis of silver-reduced graphene oxide (Ag-rgo) nanocomposite with an enhanced antibacterial effect using potamogeton pectinatus extract, RSC Adv. 5 (22) (2015) 17358–17365, https://doi.org/10.1039/c4ra13117g.
[26] M. Sedki, R.Y.A. Hassan, A. Hefnawy, I.M. El-Sherbiny, Sensing of bacterial cell viability using nanostructured bioelectrochemical system: RGO-hyperbranched chitosan nanocomposite as a novel microbial sensor platform, Sensor. Actuator. B Chem. 252 (2017), https://doi.org/10.1016/j.snb.2017.05.163.

[27] R. Forsyth, A. Devadoss, O.J. Guy, Graphene field effect transistors for biomedical applications: current status and future prospects, Diagnostics 7 (3) (2017) 45.
[28] S. Behera, S.R. Pattanaik, G. Dash, Effect of channel dimensions on transfer characteristics of graphene FET, in: 2018 IEEE Electron Devices Kolkata Conference (EDKCON), IEEE, 2018, pp. 341–343.
[29] H. Rokni, W. Lu, Layer-by-Layer insight into electrostatic charge distribution of few-layer graphene, Sci. Rep. 7 (2017) 42821.
[30] J. Zhang, H. Yang, G. Shen, P. Cheng, J. Zhang, S. Guo, Reduction of graphene oxide via L-ascorbic acid, Chem. Commun. 46 (7) (2010) 1112–1114.
[31] S. Yang, W. Yue, D. Huang, C. Chen, H. Lin, X. Yang, A facile green strategy for rapid reduction of graphene oxide by metallic zinc, RSC Adv. 2 (23) (2012) 8827–8832.
[32] P. Poulin, R. Jalili, W. Neri, F. Nallet, T. Divoux, A. Colin, S.H. Aboutalebi, G. Wallace, C. Zakri, Superflexibility of graphene oxide, Proc. Natl. Acad. Sci. Unit. States Am. 113 (40) (2016) 11088–11093.
[33] A.R. Koltonow, C. Luo, J. Luo, J. Huang, Graphene oxide sheets in solvents: to crumple or not to crumple? ACS Omega 2 (11) (2017) 8005–8009.
[34] D.K. Pandey, T.F. Chung, G. Prakash, R. Piner, Y.P. Chen, R. Reifenberger, Folding and cracking of graphene oxide sheets upon deposition, Surf. Sci. 605 (17–18) (2011) 1669–1675.
[35] S. Behura, P. Nguyen, S. Che, R. Debbarma, V. Berry, Large-area, transfer-free, oxide-assisted synthesis of hexagonal boron nitride films and their heterostructures with MoS2 and WS2, J. Am. Chem. Soc. 137 (40) (2015) 13060–13065.
[36] C.T. Thanh, N.H. Binh, N. Van Tu, V.T. Thu, M. Bayle, M. Paillet, J.L. Sauvajol, P.B. Thang, T. Dai Lam, P.N. Minh, An interdigitated ISFET-type sensor based on LPCVD grown graphene for ultrasensitive detection of carbaryl, Sensor. Actuator. B Chem. 260 (2018) 78–85.
[37] T.T. Cao, H.B. Nguyen, H.T. Bui, T.T. Vu, N.H. Phan, B.T. Phan, L. Hoang, M. Bayle, M. Paillet, J.L. Sauvajol, Fabrication of few-layer graphene film based field effect transistor and its application for trace-detection of herbicide atrazine, Adv. Nat. Sci. Nanosci. Nanotechnol. 7 (3) (2016) 35007.
[38] S. Perumbilavil, P. Sankar, T. Priya Rose, R. Philip, White light Z-scan measurements of ultrafast optical nonlinearity in reduced graphene oxide nanosheets in the 400–700 Nm region, Appl. Phys. Lett. 107 (5) (2015) 51104.
[39] K. Krishnamoorthy, M. Veerapandian, R. Mohan, S.-J. Kim, Investigation of Raman and photoluminescence studies of reduced graphene oxide sheets, Appl. Phys. A 106 (3) (2012) 501–506.
[40] M. Strankowski, D. Włodarczyk, , Piszczyk, Ł., J. Strankowska, Polyurethane nanocomposites containing reduced graphene oxide, FTIR, Raman, and XRD studies, J. Spectrosc. 2016 (2016).
[41] C. Fu, G. Zhao, H. Zhang, S. Li, Evaluation and characterization of reduced graphene oxide nanosheets as anode materials for lithium-ion batteries, Int. J. Electrochem. Sci 8 (5) (2013) 6269–6280.
[42] K.N. Kudin, B. Ozbas, H.C. Schniepp, R.K. Prud'Homme, I.A. Aksay, R. Car, Raman spectra of graphite oxide and functionalized graphene sheets, Nano Lett. 8 (1) (2008) 36–41.
[43] G. Yasin, M. Arif, M. Shakeel, Y. Dun, Y. Zuo, W.Q. Khan, Y. Tang, A. Khan, M. Nadeem, Exploring the nickel–graphene nanocomposite coatings for superior corrosion resistance: manipulating the effect of deposition current density on its morphology, mechanical properties, and erosion-corrosion performance, Adv. Eng. Mater. 20 (7) (2018) 1701166.
[44] A. Dasgupta, J. Sarkar, M. Ghosh, A. Bhattacharya, A. Mukherjee, D. Chattopadhyay, K. Acharya, Green conversion of graphene oxide to graphene nanosheets and its biosafety study, PLoS One 12 (2) (2017), e0171607.
[45] A. Jabbar, G. Yasin, W.Q. Khan, M.Y. Anwar, R.M. Korai, M.N. Nizam, G. Muhyodin, Electrochemical deposition of nickel graphene composite coatings: effect of deposition temperature on its surface morphology and corrosion resistance, RSC Adv. 7 (49) (2017) 31100–31109.
[46] S. Farah, A. Farkas, J. Madarász, K. László, Comparison of thermally and chemically reduced graphene oxides by thermal analysis and Raman spectroscopy, J. Therm. Anal. Calorim. 142 (2020) 331–337.
[47] J.I. Paredes, S. Villar-Rodil, P. Solís-Fernández, A. Martínez-Alonso, J.M.D. Tascon, Atomic force and scanning tunneling microscopy imaging of graphene nanosheets derived from graphite oxide, Langmuir 25 (10) (2009) 5957–5968.
[48] J.C. Meyer, C. Kisielowski, R. Erni, M.D. Rossell, M.F. Crommie, A. Zettl, Direct imaging of lattice atoms and topological defects in graphene membranes, Nano Lett. 8 (11) (2008) 3582–3586.
[49] Q.A. Khan, A. Shaur, T.A. Khan, Y.F. Joya, M.S. Awan, Characterization of reduced graphene oxide produced through a modified hoffman method, Cogent Chem 3 (1) (2017) 1298980.
[50] A.C. Ferrari, J. Robertson, Interpretation of Raman spectra of disordered and amorphous carbon, Phys. Rev. B 61 (20) (2000) 14095.
[51] R. Blume, P.R. Kidambi, B.C. Bayer, R.S. Weatherup, Z.-J. Wang, G. Weinberg, M.-G. Willinger, M. Greiner, S. Hofmann, A. Knop-Gericke, The influence of intercalated oxygen on the properties of graphene on polycrystalline Cu under various environmental conditions, Phys. Chem. Chem. Phys. 16 (47) (2014) 25989–26003.
[52] M.K. Rabchinskii, S.A. Ryzhkov, D.A. Kirilenko, N.V. Ulin, M.V. Baidakova, V.V. Shnitov, S.I. Pavlov, R.G. Chumakov, D.Y. Stolyarova, N.A. Besedina, From graphene oxide towards aminated graphene: facile synthesis, its structure and electronic properties, Sci. Rep. 10 (1) (2020) 1–12.
[53] A. Ganguly, S. Sharma, P. Papakonstantinou, J. Hamilton, Probing the thermal deoxygenation of graphene oxide using high-resolution in situ X-ray-based spectroscopies, J. Phys. Chem. C 115 (34) (2011) 17009–17019.
[54] J. Jo, S. Lee, J. Gim, J. Song, S. Kim, V. Mathew, M.H. Alfaruqi, S. Kim, J. Lim, J. Kim, Facile synthesis of reduced graphene oxide by modified hummer's method as anode material for Li-, Na-and K-ion secondary batteries, R. Soc. open Sci. 6 (4) (2019) 181978.
[55] A. Lerf, H. He, M. Forster, J. Klinowski, Structure of graphite oxide revisited, J. Phys. Chem. B 102 (23) (1998) 4477–4482.
[56] T. Szabó, O. Berkesi, P. Forgó, K. Josepovits, Y. Sanakis, D. Petridis, I. Dékány, Evolution of surface functional groups in a series of progressively oxidized graphite oxides, Chem. Mater. 18 (11) (2006) 2740–2749.
[57] W. Gao, L.B. Alemany, L. Ci, P.M. Ajayan, New insights into the structure and reduction of graphite oxide, Nat. Chem. 1 (5) (2009) 403.
[58] M. Khandelwal, A. Kumar, One-step chemically controlled wet synthesis of graphene nanoribbons from graphene oxide for high performance supercapacitor applications, J. Mater. Chem. 3 (45) (2015) 22975–22988.
[59] I.A. Vacchi, C. Spinato, J. Raya, A. Bianco, C. Ménard-Moyon, Chemical reactivity of graphene oxide towards amines elucidated by solid-state NMR, Nanoscale 8 (28) (2016) 13714–13721.
[60] S. Park, Y. Hu, J.O. Hwang, E.S. Lee, L.B. Casabianca, W. Cai, J.R. Potts, H.W. Ha, S. Chen, J. Oh, Chemical structures of hydrazine-treated graphene oxide and generation of aromatic nitrogen doping, Nat. Commun. 3 (2012) 638.
[61] H.W. Kim, H. Park, J.S. Roh, J.E. Shin, T.H. Lee, L. Zhang, Y.H. Cho, H.W. Yoon, V.J. Bukas, J. Guo, Carbon defect characterization of nitrogen-doped reduced graphene oxide electrocatalysts for the two-electron oxygen reduction reaction, Chem. Mater. 31 (11) (2019) 3967–3973.
[62] A. Lipatov, M.J.-F. Guinel, D.S. Muratov, V.O. Vanyushin, P.M. Wilson, A. Kolmakov, A. Sinitskii, Low-temperature thermal reduction of graphene oxide: in situ correlative structural, thermal desorption, and electrical transport measurements, Appl. Phys. Lett. 112 (5) (2018) 53103.
[63] M. Acik, G. Lee, C. Mattevi, A. Pirkle, R.M. Wallace, M. Chhowalla, K. Cho, Y. Chabal, The role of oxygen during thermal reduction of graphene oxide studied by infrared absorption spectroscopy, J. Phys. Chem. C 115 (40) (2011) 19761–19781.
[64] S. Tian, J. Sun, S. Yang, P. He, S. Ding, G. Ding, X. Xie, Facile thermal annealing of graphite oxide in air for graphene with a higher C/O ratio, RSC Adv. 5 (85) (2015) 69854–69860.
[65] D. Krishnan, F. Kim, J. Luo, R. Cruz-Silva, L.J. Cote, H.D. Jang, J. Huang, Energetic graphene oxide: challenges and opportunities, Nano Today 7 (2) (2012) 137–152.
[66] L. Klemeyer, H. Park, J. Huang, Geometry-dependent thermal reduction of graphene oxide solid, ACS Mater. Lett. 3 (2021) 511–515.
[67] A. Bagri, R. Grantab, N.V. Medhekar, V.B. Shenoy, Stability and formation mechanisms of carbonyl-and hydroxyl-decorated holes in graphene oxide, J. Phys. Chem. C 114 (28) (2010) 12053–12061.
[68] A. Bagri, C. Mattevi, M. Acik, Y.J. Chabal, M. Chhowalla, V.B. Shenoy, Structural evolution during the reduction of chemically derived graphene oxide, Nat. Chem. 2 (7) (2010) 581–587.
[69] A.F. da Silva, A.M. Christmann, T.M.H. Costa, A.R. Muniz, N.M. Balzaretti, Thermal annealing of graphite oxide under high pressure: an experimental and computational study, Carbon N. Y. 139 (2018) 1035–1047.
[70] M.A. Velasco-Soto, S.A. Pérez-García, J. Alvarez-Quintana, Y. Cao, L. Nyborg, L. Licea-Jiménez, Selective band gap manipulation of graphene oxide by its reduction with mild reagents, Carbon N. Y. 93 (2015) 967–973.
[71] L. Ci, L. Song, C. Jin, D. Jariwala, D. Wu, Y. Li, A. Srivastava, Z.F. Wang, K. Storr, L. Balicas, Atomic layers of hybridized boron nitride and graphene domains, Nat. Mater. 9 (5) (2010) 430–435.
[72] H. Huang, Z. Li, J. She, W. Wang, Oxygen density dependent band gap of reduced graphene oxide, J. Appl. Phys. 111 (5) (2012) 54317.
[73] P. Sehrawat, S.S. Islam, P. Mishra, S. Ahmad, Reduced graphene oxide (RGO) based wideband optical sensor and the role of temperature, defect states and quantum efficiency, Sci. Rep. 8 (1) (2018) 1–13.
[74] M.T. Hasan, B.J. Senger, C. Ryan, M. Culp, R. Gonzalez-Rodriguez, J.L. Coffer, A.V. Naumov, Optical band gap alteration of graphene oxide via ozone treatment, Sci. Rep. 7 (1) (2017) 1–8.
[75] U.A.M. Romero, M.Á.V. Soto, L.L. Jiménez, J.Á. Quintana, S.A.P. García, Graphene derivatives: controlled properties, nanocomposites, and energy harvesting applications, Graphene Mater. Prop. Modif. (2017).
[76] L. Liu, J. Zhang, H. Gao, L. Wang, X. Jiang, J. Zhao, Tailoring physical properties of graphene: effects of hydrogenation, oxidation, and grain boundaries by atomistic simulations, Comput. Mater. Sci. 112 (2016) 527–546.
[77] M. Lundie, , Šljivančanin, Ž., S. Tomić, Electronic and optical properties of reduced graphene oxide, J. Mater. Chem. C 3 (29) (2015) 7632–7641.
[78] P.V. Kumar, M. Bernardi, J.C. Grossman, The impact of functionalization on the stability, work function, and photoluminescence of reduced graphene oxide, ACS Nano 7 (2) (2013) 1638–1645.
[79] Y. Jin, Y. Zheng, S.G. Podkolzin, W. Lee, Band gap of reduced graphene oxide tuned by controlling functional groups, J. Mater. Chem. C 8 (14) (2020) 4885–4894.
[80] R.J. Martín-Palma, J. Martínez-Duart, Nanotechnology for Microelectronics and Photonics, Elsevier, 2017.
[81] M. Javaid, D.W. Drumm, S.P. Russo, A.D. Greentree, A study of size-dependent properties of MoS 2 monolayer nanoflakes using density-functional theory, Sci. Rep. 7 (1) (2017) 1–11.
[82] B. Delley, E.F. Steigmeier, Size dependence of band gaps in silicon

nanostructures, Appl. Phys. Lett. 67 (16) (1995) 2370–2372.
[83] X. Dong, W. Huang, P. Chen, In situ synthesis of reduced graphene oxide and gold nanocomposites for nanoelectronics and biosensing, Nanoscale Res Lett 6 (1) (2011) 1–6.
[84] J. Yang, J. Kim, H.S. Shin, Facile method for RGO field effect transistor: selective adsorption of RGO on SAM-treated gold electrode by electrostatic attraction, Adv. Mater. 24 (17) (2012) 2299–2303.
[85] I.-Y. Sohn, D.-J. Kim, J.-H. Jung, O.J. Yoon, T.N. Thanh, T.T. Quang, N.-E. Lee, PH sensing characteristics and biosensing application of solution-gated reduced graphene oxide field-effect transistors, Biosens. Bioelectron. 45 (2013) 70–76.
[86] C. Gómez-Navarro, R.T. Weitz, A.M. Bittner, M. Scolari, A. Mews, M. Burghard, K. Kern, Electronic transport properties of individual chemically reduced graphene oxide sheets, Nano Lett. 7 (11) (2007) 3499–3503.
[87] S. Tian, J. Sun, S. Yang, P. He, G. Wang, Z. Di, G. Ding, X. Xie, M. Jiang, Controllable edge oxidation and bubbling exfoliation enable the fabrication of high quality water dispersible graphene, Sci. Rep. 6 (2016) 34127.
[88] M.A. Uddin, N. Glavin, A. Singh, R. Naguy, M. Jespersen, A. Voevodin, G. Koley, Mobility enhancement in graphene transistors on low temperature pulsed laser deposited boron nitride, Appl. Phys. Lett. 107 (20) (2015) 203110.
[89] B. Zhang, W.H. Lee, R. Piner, I. Kholmanov, Y. Wu, H. Li, H. Ji, R.S. Ruoff, Low-temperature chemical vapor deposition growth of graphene from toluene on electropolished copper foils, ACS Nano 6 (3) (2012) 2471–2476.
[90] G. Wang, M. Zhang, Y. Zhu, G. Ding, D. Jiang, Q. Guo, S. Liu, X. Xie, P.K. Chu, Z. Di, Direct growth of graphene film on germanium substrate, Sci. Rep. 3 (2013) 2465.
[91] A. Zak, M.A. Andersson, M. Bauer, J. Matukas, A. Lisauskas, H.G. Roskos, J. Stake, Antenna-integrated 0.6 THz FET direct detectors based on CVD graphene, Nano Lett. 14 (10) (2014) 5834–5838.
[92] D.B. Farmer, H.-Y. Chiu, Y.-M. Lin, K.A. Jenkins, F. Xia, P. Avouris, Utilization of a buffered dielectric to achieve high field-effect carrier mobility in graphene transistors, Nano Lett. 9 (12) (2009) 4474–4478.
[93] S.S. Sukumaran, S. Tripathi, A.N. Resmi, K.G. Gopchandran, K.B. Jinesh, Influence of surfactants on the electronic properties of liquid-phase exfoliated graphene, Mater. Sci. Eng. B 240 (2019) 62–68.